Numerical Determination of the Volumetric Heat Transfer Coefficient in Fixed Beds of Wood Chips

Vasileios Sassanis, Lionel Gamet, Matthieu Rolland, Ruoyi Ma, Victor Pozzobon

HAL Id: hal-03287011
https://ifp.hal.science/hal-03287011

Submitted on 15 Jul 2021

Numerical determination of the volumetric heat transfer coefficient in fixed beds of wood chips

Vasileios Sassanis[1], Lionel Gamet[1], Matthieu Rolland[1], Ruoyi Ma[1], and Victor Pozzobon[2] ✉

[1]IFP Energies nouvelles, Rond-Point de l'échangeur de Solaize, BP3, 69360 Solaize, France
[2]LGPM, CentraleSupélec, Université Paris-Saclay, SFR Condorcet FR CNRS 3417, Centre Européen de Biotechnologie et de Bioéconomie (CEBB), 3 rue des Rouges Terres 51110 Pomacle, France

The aim of this work is to build CFD tools to study heat transfer in packed beds during the thermochemical upgrading process of woody biomass. For that purpose, a numerical workflow capable of investigating heat transfer phenomena inside a packed bed was developed. First, the bed is generated using a Discrete Element Method (DEM) code. Then, a steady-state Direct Numerical Simulation (DNS) solver is used to acquire the flow patterns inside the pores of the bed. Finally, the heat equation is solved for the particles and the fluid in a coupled manner. The results are thoroughly validated against two benchmark cases: flow around a sphere and flow through a packed bed of spheres. The importance of accounting for internal heat resistance for substrates with high Biot number (e.g. wood) is highlighted. Furthermore, the heat transfer phenomena inside a packed bed of torrefied wood chips are investigated. Values of the heat transfer coefficient are also provided ($\simeq$5 W/m^2/K, for Re < 5, 7.7 for Re=10). Another interesting finding is the effect of channeling in this type of beds and its impact on the temperature field of the wood chips.

Fixed bed | Heat transfer | DEM | CFD | OpenFOAM
Correspondence: *victor.pozzobon@centralesupelec.fr*

1. Introduction

Lignocellulosic biomass is a high-quality, second-generation biofuel production element (1–3). Through various thermochemical upgrading processes, mainly pyrolysis and gasification, it can produce a wide variety of products (e.g. char, producer gas, syngas, bio-oils). From an engineering perspective, the quality of those products strongly depends on the initial substrate properties as well as on the process specifications (temperature, heating rate and catalyst type) (4). In addition, it is widely understood that controlled pretreatment steps, such as drying, torrefaction, grinding and pelletization improve the overall process throughput (5).

Grinding and pelletization help in standardizing the substrate dimensions, ensuring that all particles undergo similar heat treatment. Drying makes the substrate lighter and prevents microbiological degradation of the biomass. Torrefaction offers valuable properties to the substrate, namely, hydrophobicity and higher energy density (6). The thermochemical conversion steps follow, with pyrolysis being the first one. Pyrolysis break down biomass into three broad fractions: char, tar and gas. As mentioned earlier, temperature and heating rate play an important role on the quality of these products. Finally, gasification (or oxidative gasification, depending on the process design) upgrades pyrol-

ysis products to producer gas, which can also be later upgraded into syngas. In most cases, when the upgrading process does not require high heating rates, fixed bed reactors are employed for biomass conversion. This technology is now well-established, robust and versatile, constituting an excellent option for biomass conversion (7–15).

The fixed bed is created by inserting the biomass into a designated container. The heating strategies vary depending on the purpose. From a scientific point of view, as one may not want to dilute the products with combustion fumes, an allothermal operation is chosen. In this case, heat can originate from different sources: controlled temperature gas blown thought the bed, electrical heating (16), radiative/solar heating (17), to name a few. In an industrial environment, most of the time air is sent into the reactor in order to oxidize part of the biomass and generate heat *in situ*, leading to an autothermal process.

In all of the above fixed bed configurations, ensuring proper heating of the substrate is of great importance. For large chips or high gas/solid temperature differences, the question of thermal uniformity of the chips inside the bed remains. Indeed, as biomass is a poor heat conducting material, a significant amount of time may be needed for the core of the chips to reach temperatures comparable to the one of their periphery. In addition, as they are reactive, subject to either endothermic of exothermic reactions, their perfect thermal homogeneity is only theoretically viable. This is crucial given the fact that conversion reactions and their products strongly depend on the thermal history of the particles (18). A strategy to limit this kind of problem is to grind the biomass to very fine levels. This, however, doubles the operational cost due to the grinding and the decrease of the bed permeability which results in higher gas pumping costs. In addition, from a process perspective, handling powders is far more complicated than chips or pellets. Knowing the volumetric heat transfer coefficient between gas and solid in this kind of configurations would be of help in assessing the impact of the aforementioned phenomena and to better control the process. Yet, obtaining the heat transfer coefficient in complex geometries such as a fixed bed of wood chips is experimentally challenging. Typically, other researchers rely on correlations linking Nusselt, Reynolds and Prandtl numbers, derived on multiple objects with different shapes (19–21). The most famous of those correlations is the one proposed by Whitaker, where the particles' shape is taken into account via bed porosity (22).
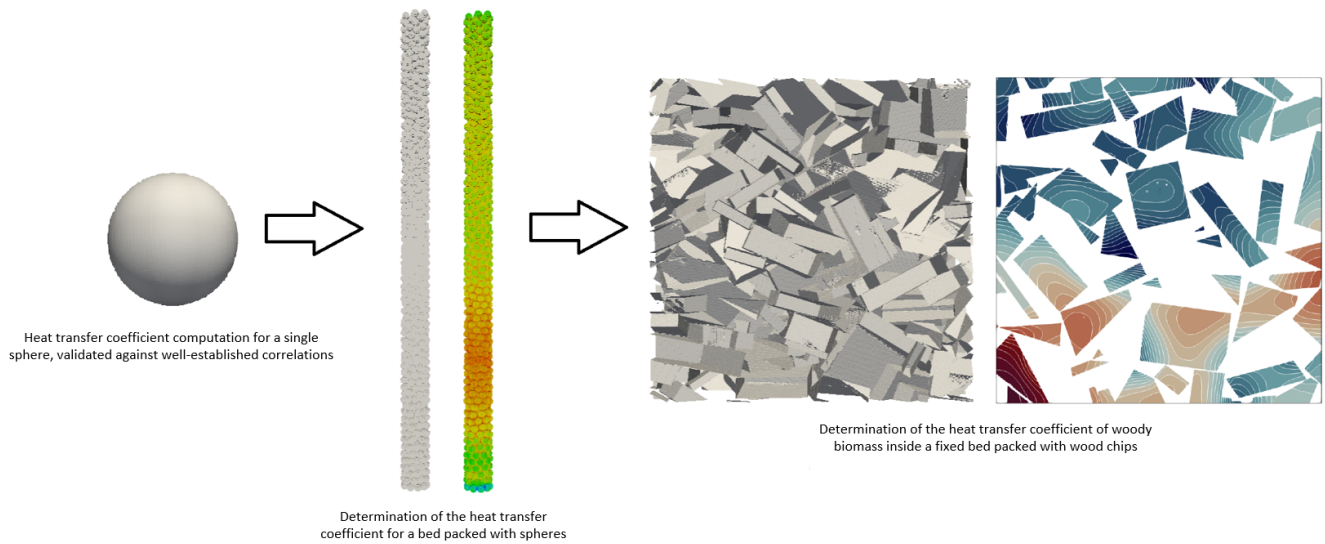
Graphical abstract

Even though those correlations are of help, engineers and scientists are lacking an optimal way of determining the heat transfer coefficient inside the bed. Furthermore, an assessment of the impact of wood chips poor thermal conductivity is also missing from the literature. In this context, the objective of this work is to acquire the volumetric heat transfer coefficient of a fixed bed from fluid flow computation in-between the particles. Computing macroscopic physical properties based on accurate description of microscopic phenomena is not a new idea. It has been made available over the past decade thanks to the increase in computational power. It has successfully been applied to granular media, rocks permeability determination (23–25), heat exchanger (26) or static mixer design (27, 28).Their application to fixed beds has been recently and extensively reviewed by Jurtz (29). To date, authors working on fixed bed simulations tackle diverse challenges, such as dealing with geometries more complex than sphere packings (30–33), solving more complex physics such as natural convection (34) or radiation (35), and coupling with complex chemistry (36, 37).

In our case, a CFD code computing fluid flow and heat transfer both inside the fluid and the particles is proposed. As a first step, this tool is validated against well-established correlations, first for a single sphere, then for a fixed bed made of spheres. To do so, a DEM code is used to numerically generate a fixed bed of spheres for the CFD code. A full, novel workflow is employed for the generation and characterization of a packed bed of wood chips. This application appears all the more relevant as wood chips feature an intermediate Biot number, preventing classical decoupling between internal and external heat transfer. Finally, on a practical level, this workflow is freely accessible on an online repository.

2. Numerical methods

The volumetric heat transfer coefficient is investigated in steady-state over different geometries. A single-sphere setup and various setups of multiple spheres were investigated and compared against the existing extensive literature data. Among the numerous articles, the terminology of the well-established review from Whitaker (22) is adopted in this paper, dealing, among others, with the heat transfer coefficient in fixed beds of non-spherical particles. To do so, bed geometries were first generated using DEM, then, fluid flow and heat transfer were computed inside those geometries before extracting heat transfer coefficients.

2 1. Beds generation process

The numerical fixed beds of spheres for validation have been produced using an in-house code called Grains3D, based on the Discrete Element Method (DEM) (38) that solves inelastic collisions between particles. It uses the Gilbert–Johnson–Keerthi (GJK) algorithm (39) to detect collisions and compute contact forces and momentum. More details on Grains3D and its validation on convex particles and workflow can be found in (40, 41). For the cases presented here, the spheres were introduced one by one at random locations in an insertion box located in the upper part of the cylindrical reactor. Then, they fall due to gravity (g = 9.81 m/s^2) and collide with the bottom plate, the cylindrical reactor or other particles. The simulations were stopped when the kinetic energy was dissipated and the particles stopped moving. Finally, spheres' locations were exported to OpenFOAM to recreate the fixed bed geometry.

Similar to the packing of spheres, numerical details regarding the wood chips bed generation procedure can be found in the literature (42) and will only be briefly summarized here. 536 wood chips, selected randomly, were measured in 3D using a caliper. Population convergence has also been ensured. They were then reproduced numerically as parallelepipeds and randomly duplicated to a 15000 particle population. The bed was generated by computing the stack of these randomly oriented particles into a cylinder using the

open source LMGC90 DEM code (43)[1]. This code was chosen as LMGC90 is among the codes that can handle polyhedral collision detection and contact point friction without emulating solids with a group of spheres (44).

2 2. Fluid flow and heat transfer models

The case is examined in steady-state. The fluid flow is considered incompressible and laminar. Heat transfer is described using conduction in both phases and convection in fluid phase. Furthermore, as the motion can be considered as forced convection, the coupling between density and temperature is neglected. Thus, the following set of equations is obtained for the fluid phase: classical Navier-Stokes equations, i.e. continuity (Eq. 1) and momentum conservation (Eq. 2).

$$\nabla.\boldsymbol{u} = 0 \tag{1}$$

$$\boldsymbol{u}\nabla.\boldsymbol{u} = -\frac{\nabla P}{\rho} + \nu\nabla^2\boldsymbol{u} \tag{2}$$

Heat transfer balance is derived in both fluid and solid phases. In both cases, it is used in its most classical form featuring heat convection and conduction for the fluid (Eq. 3) and conduction and volumetric heat release (ω) for the solid (Eq. 4).

$$\nabla(\boldsymbol{u}c_p T_f) = -\nabla.(-k_f\nabla T_f) \tag{3}$$

$$0 = -\nabla.(-k_p\nabla T_p) + \omega_p \tag{4}$$

The boundary conditions between the solid and fluid domains are simple. From a fluid flow perspective, the solid domain is considered as a wall, i.e. zero velocity and normal pressure gradient. Heat transfer boundary conditions are based on heat flux conservation at the interface, meaning that the two temperatures are equal (Eq. 5) and the heat flux has the same value on both sides (Eq. 6).

$$T_f\big|_{wall} = T_p\big|_{wall} \tag{5}$$

$$-k_p\nabla T_p\big|_{wall} = -k_f\nabla T_f\big|_{wall} \tag{6}$$

Figure 1 provides a schematic of the cases with the associated boundary conditions for the single sphere configuration. The values of the physical properties are available in Table 1. The fluid properties are close to those of air while particle properties are close to those of beech wood (*Fagus sylvatica*), except for the thermal conductivity taken as the one of steel to ensure better agreement with experiments. Still, in this kind of computations, dimensionless numbers are more important than absolute values. In this case, the fluid Prandtl number is close to 0.5, meaning that momentum and temperature boundary layers are of the same order of magnitude. In addition, with the highest value of convective heat transfer

[1]It is worth noting that both DEM codes could handle the generation of the two types of beds. The interested reader can apply the workflow and reproduce this work on any of the two.

Property	Fluid	Particle
ρ, kg/m^3	1.2	750
c_p, J/kg/K	1004	1500
k, W/m/K	0.026	100
ν, m^2/s	$1.00\ 10^{-5}$	-
Pr	0.463	-
ω, W/m^3	-	$1.00\ 10^6$

Table 1. Physical properties used for the validation cases

coefficient (h) being approximately 35 W/m^2/K, the particle Biot number (Eq. 7) presents a maximum value of $1.05\ 10^{-3}$, i.e. far below 0.1, thanks to the artificially high solid-thermal conductivity. This ensures thermal uniformity which allows for reasonable comparisons with experimental studies conducted with spheres of constant temperature.
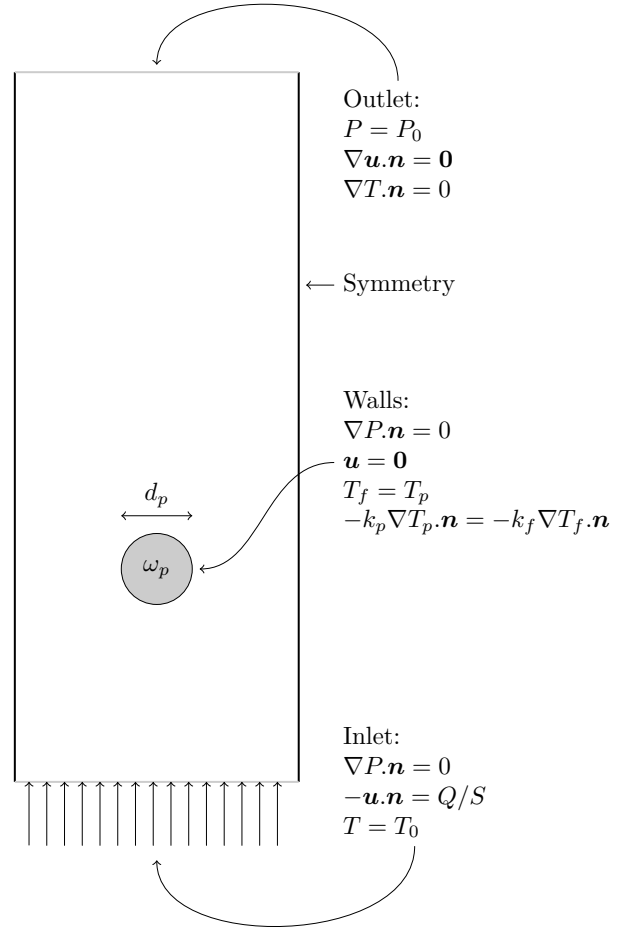

Fig. 1. Numerical setup for the single sphere case

$$Bi = \frac{h\,d_p}{k_p} \tag{7}$$

2 3. Numerical methods for fluid flow and heat transfer computations

The fluid flow and heat transfer equations were implemented with the OpenFOAM C++ open-source library (45). The

Case number	Number of cells per particle diameter	Additional local refinement level Particle	Reactor wall	Number of cells (millions)
1	10	1	1	0.99
2	10	1+	1+	2.35
3	10	2	2	3.91
4	20	1	1+	3.19
5	20	1+	1+	5.36
6	25	1+	1+	7.31
7	30	1	0	5.86
8	30	1	1	6.85
9	30	1+	0	7.54
10	30	1+	1+	9.66

Table 2. Mesh generation parameters for convergence analysis. 1+: local refinement of 2 near sharp edges (angle > 30°), 1 everywhere else

solver is a multi-region solver using two grid regions, one for the fluid and one for the solid. Equations were discretized using second order off-centered schemes for convection terms and centered schemes for diffusion ones. Fluid flow is solved using SIMPLEC scheme (46). As temperature has no retroaction on fluid properties, a segregated solving strategy was used. Once the fluid flow has been obtained, the heat transfer equation is solved for both the fluid and solid regions.

While mesh generation is rather easy for the single sphere setup and can be handled by a human operator, it becomes complex for intricated geometries such as packed beds and has to be delegated to a specialized meshing algorithm. In this case, OpenFOAM automatic mesher, *snappyHexMesh*, was used. Briefly, a hexahedral background mesh is supplied to the algorithm which will then detect cells intersected by the particle walls and mark those as to be refined. In regions where a higher level of refinement is specified (on particle walls or in small gap regions between particles), *snappyHexMesh* splits the cells in 2 in all directions. One level of refinement corresponds to a division of cells by 8, two levels of refinement to a division by 64, and so on. A surface-based refinement level (typically 1 or 2) is used on all the surfaces of the spheres. A global *gapLevelIncrement* (value 1) was used to ensure the proper treatment of the thin gaps in regions where the spheres are tangent. Once completed, divided cells are snapped onto the geometry surface in order to faithfully reproduce the physical geometry. More details for the grid generation procedure can be found in (42).

Mesh independence is very important for such an investigation occurring in complex geometries. To ensure mesh independence several combinations of the meshing algorithm parameters were tested (Table 2) at the bed level for a Reynolds number equal to 30. Following this procedure for a high Reynolds number value guarantees that boundary layers are properly captured and will be properly accounted for in lower Reynolds number cases, as the boundary layer gets wider. Three criteria were used to assess mesh convergence: numerical accuracy on the particle volume as it impacts both fluid flow and heat generation (Fig. 2 (a)), outlet temperature (with respect to the theoretical value deduced from heat balance, Fig. 2 (b)) and total heat flux (with respect to experimental correlation, Fig. 2 (c)).

From these results, the meshing strategy used for the mesh

number 5 was finally selected as it produced very satisfying results. With this strategy, meshing a bed made of 60 spheres required about 3 million cells, resulting in a case run time of 3h on 72 processors (Intel Skylake G-6140 @ 2.3 GHz, 1 cluster node: 96 GB memory + 2 processors per node, 18 cores per processor).

2 4. Case setup & Volumetric heat transfer coefficient determination

The workflow validation followed an incremental procedure. First, its predictions were validated against the well-established case of one single sphere in an infinite medium. Second, they were validated against the case of a fixed bed made of spheres. Detailed case setups and the associated boundary conditions are presented in Table 3.

The determination of the heat transfer coefficient depends on the case setup. In the first case, it can be determined using Eq. 8. One should note that the maximum sphere temperature has to be used in order to properly account for the coefficient. Indeed, as documented by Grace and Clift (47), temperature minimum is located upstream and maximum downstream. The fluid wake temperature can be higher than the average fluid temperature. Using an average temperature would lead to non-physical behavior as the fluid wake temperature can be higher than the average sphere temperature. This would mean that the fluid would heat up the sphere, creating an artifact.

$$h = \frac{\omega_p V_p}{S_p(T_{f,in} - T_{p,max})} \tag{8}$$

While reasonably straightforward for the single sphere case, the fixed bed heat transfer coefficient is somewhat more demanding. Indeed, the formulations used to obtain the volumetric heat transfer coefficient experimentally assume that T_f and T_p only depend on the z coordinate. However, the actual temperature field is 3D, meaning that they have to be averaged. For the fluid temperature, the mixing cup temperature is used, defined as the velocity weighted temperature. The solid temperature is almost uniform, owing to its high thermal conductivity. Hence, the maximum value is employed to ensure that the temperature difference is always positive and h can be correctly computed.
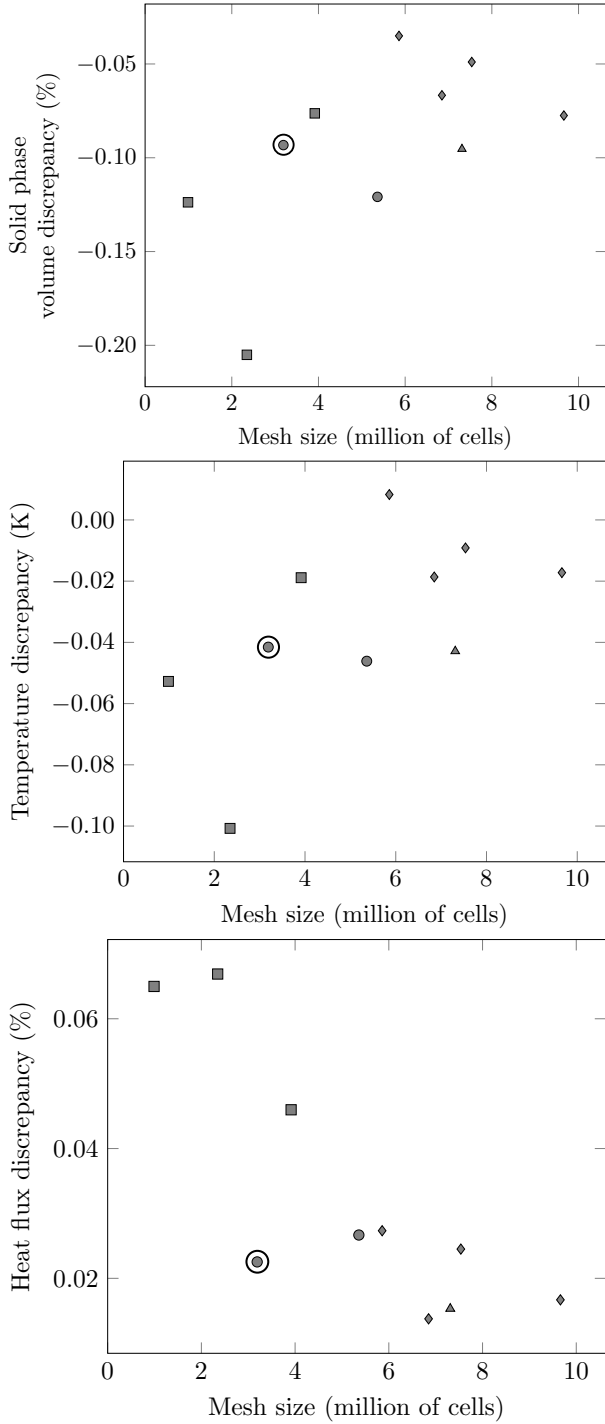
Fig. 2. Mesh convergence analysis results: top - solid phase volume, middle - temperature discrepancy, bottom - heat flux d iscrepancy. M arkers: s quare - base mesh d_p/10, circle - base mesh d_p/20, triangle - base mesh d_p/25, diamonds - base mesh d_p/30. For each base mesh, increasing refinement l evels were tested. Chosen mesh: circled one

As demonstrated by Wakao (48), a proper estimation of the heat transfer coefficient requires to account for heat conductivity in the fluid. Integration of the heat equation in the fixed bed (Eq. 9) along the bed length gives an expression of the heat transfer coefficient (Eq. 10).

$$k_f \frac{d^2(T_f - T_p)}{d^2 z} - \rho_f c_{pf} \frac{|\boldsymbol{u}|}{\epsilon} \frac{d(T_f - T_p)}{dz}$$
$$- \frac{h a_{bed}}{\epsilon}(T_f - T_p) = 0 \quad \textbf{(9)}$$

This equation can be solved analytically by integrating between the inlet and the outlet, yielding the convective heat transfer coefficient:

$$h = -\frac{\rho_f c_{pf} |\boldsymbol{u}|}{L_{bed} a_{bed}} \ln\left(\frac{\Delta T_{bed,out}}{\Delta T_{bed,in}}\right) + \frac{\epsilon k_f}{L_{bed}^2 a_{bed}} \ln^2\left(\frac{\Delta T_{bed,out}}{\Delta T_{bed,in}}\right)$$
$$\textbf{(10)}$$

where, for example, $\Delta T_{bed,in}$ is the fluid particle temperature difference at the inlet of the bed: $\Delta T_{bed,in} = T_{f,bed,in} - T_{p,bed,in}$.

3. Test cases results

3 1. Single sphere case

Figure 3 presents the contours of the flow temperature for the single sphere test case. As one can observe, the temperature field features a sharp gradient over the part facing the flow and a smoother one in the wake. Special care was taken in selecting the computational domain size. Indeed, as symmetry boundary conditions are used to describe the lateral boundary, they would act as infinitely repeating spheres that could perturb the simulated one. This would be true especially at low Reynolds numbers . Thus, an analysis on the impact of the domain size was conducted. For a given Reynolds number of 1 (lowest value of the examined range), the domain diameter was increased progressively from 30 mm until the obtained Nusselt number was stabilized. Stabilization occurred for a domain size with a diameter of 60 mm. Thus, it can be concluded that for this Reynolds number, computational domain independence is achieved. As the Reynolds number was the lowest one, this configuration is the most conservative in terms of lateral flux perturbations on the solution and will be kept for the rest of the study.

To assess the quality of the procedure, results are compared with the correlations from the literature (Whitaker (22), Clift (47), Feng (49), Ranz Marshall (50)). Comparisons are reported in Figure 4. The proposed solver compares very well with the results obtained from the evaluation of the correlation. Furthermore, the results are particularly close to those reported by Whitaker. This illustrates the quality of the workflow as Whitaker's correlation is fitted over experimental data obtained for low Reynolds number values. Evidently, for the single sphere case, the solver gives results in good agreement with the experiments.

3 2. Packed bed of multiple spheres

Figure 5 presents the contours of the flow temperature for the fixed bed of spheres. It can be noted that thermal boundary layers merge quite soon after entering the bed. This observation enhances the need for proper mathematical treatment,

	Single sphere	Fixed bed of spheres
Inlet	Flow: uniform velocity Temperature: uniform temperature	
Outlet	Flow: uniform pressure Temperature : no gradient	
Lateral boundary condition	Flow: Slip condition Temperature: No gradient	Flow: No-Slip condition Temperature: No gradient
Reynolds number	$\dfrac{d_p\|\boldsymbol{u}\|}{\nu}$	$\dfrac{d_p\|\boldsymbol{u}\|}{\nu(1-\epsilon)}$
Convective heat transfer coefficient	$\dfrac{\omega_p V_p}{S_p(T_{f,in}-T_{s,max})}$	$-\dfrac{\rho_f c_{pf}\|\boldsymbol{u}\|}{L_{bed}a_{bed}}\ln(\dfrac{\Delta T_{bed,out}}{\Delta T_{bed,in}})+\dfrac{\epsilon k_f}{L_{bed}^2 a_{bed}}\ln^2(\dfrac{\Delta T_{bed,out}}{\Delta T_{bed,in}})$
Nusselt number	$\dfrac{hd_p}{k_f}$	$\dfrac{hd_p}{k_f}\dfrac{\epsilon}{1-\epsilon}$
Whitaker's Correlation	$\mathrm{Nu} = 2 + (0.4\,\mathrm{Re}^{1/2} + 0.06\,\mathrm{Re}^{2/3})\,\mathrm{Pr}^{2/5}$	$\mathrm{Nu} = (0.5\,\mathrm{Re}^{1/2} + 0.2\,\mathrm{Re}^{2/3})\,\mathrm{Pr}^{1/3}$
Case geometry	1 sphere in a large cylinder d_p = 3 mm $L_{cylinder}$ = 27 d_p = 81 mm $d_{cylinder}$ = 20 d_p = 60 mm Sphere position: 7 d_p from the inlet	61 spheres in a cylinder d_p = 3 mm L_{bed} = 17.6 mm $d_{cylinder}$ = 12 mm a_{bed} = 863 m^2/m^3 ϵ = 0.57 For Re < 10: $L_{cylinder}$ = 65 mm Bed position: 29.5 mm from the inlet For Re $\geq$ 10: $L_{cylinder}$ = 52 mm Bed position: 16.5 mm from the inlet

Table 3. Case setup for each validation run, dimensionless numbers definitions and benchmark correlations.
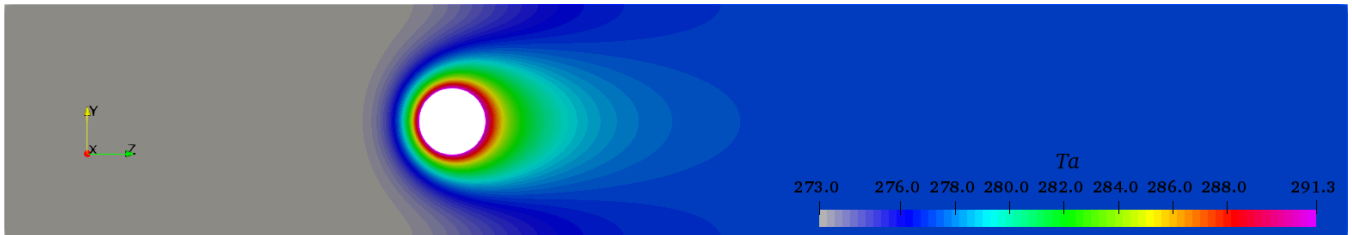

Fig. 3. Heat map in the fluid region (truncated laterally for publication purposes). Case setup: 3 mm diameter sphere, Re = 10, ω = 10^6 W/m^3, fluid inlet temperature: air at 273 K, flow from left to right

as proposed by Wakao (48). A quantitative comparison was conducted with Whitaker's correlation (available in Tab. 3) for a fixed bed made of spheres. Results are displayed in Figure 6.

Very good agreement is observed starting from a Reynolds number of 7 and on, which is very good as Whitaker himself states that his correlation provides satisfactory results for Re = 50 and above. In addition, Whitaker also underlined that the log-log plots tend to minimize the perception of the experimental data spread (around $\pm$ 25 %). This is why results are plotted with a shaded area of this magnitude. As one can see, they are well encompassed in the suggested $\pm$ 25 % range.

The above observations prove that the model of global heat transfer coefficient and the multi-region solver together provide satisfactory modeling of the macroscopic heat transfer phenomenon, for Reynolds numbers in the range of 7 to 70 (corresponding to Reynolds numbers from 3 to 30, with a more classic definition based on the raw particle diameter).

4. Comments on particle internal heat transfer

In the proposed workflow, the particle internal heat transfer is accounted for. This kind of description was chosen
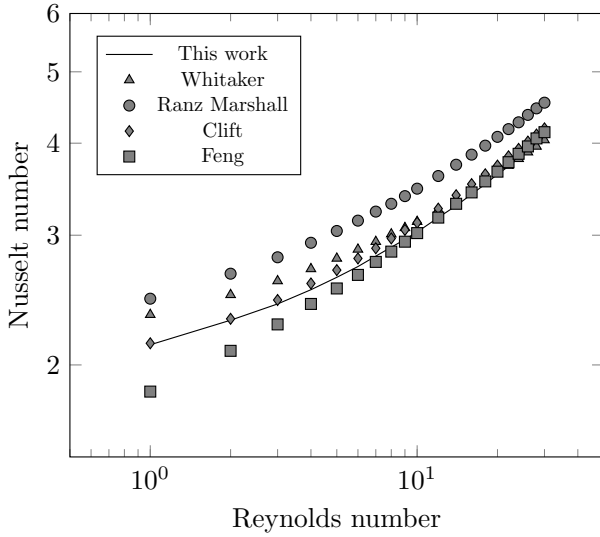
Fig. 4. Nusselt number predicted versus Reynolds number for the single sphere case.

is normal. Indeed, as the simulations run in steady state, the overall averaged fluid temperature increase is tied to the heat released by the sphere, which is the same for all configurations. On the contrary, the slower fluid temperature rise can be explained by a less efficient overall heat transfer process from the sphere to the fluid. In the case of spheres with Biot number of 0.6, both internal and external heat transfer resistance come into play. While, in the low Biot number case only the external one was limiting transfer. With the fluid flow being the same for all setups, the discrepancy can be attributed to the internal heat transfer resistance solely. This observation highlights the importance of properly accounting for solid internal heat transfer in high Biot number configurations.

5. Fixed bed of wood chips

In order to illustrate the capabilities of the proposed workflow, the case of the cooldown of freshly torrefied wood chips inspired by Bouzarour's work (52) is selected. Briefly, wood chips were poured into a reactor and torrefied at a temperature of 285 °C for two hours before being cooled down. As it is more reactive than untreated wood, torrefied wood can be subject to self-heating when exposed to oxygen even at moderate temperatures. The referred (52) study analyzed the impact of air injection at a temperature of 150 °C. Indeed, the earlier air is introduced in the cooldown process, the lower the costs compared to pure nitrogen flushing. These experiments were carried out for three different flow rates, 10, 20 and 30 NL/min corresponding to 50, 100 and 150 % of the maximal recommendation for this configuration (53). The authors have been able to determine the heat release associated to the phenomena and to produce a correlation for it (Eq. 11)(52). This illustration case is particularly interesting because it features both internal and external heat transfer resistance and a source term highly dependent to temperature.

as it is closer to the actual physical phenomenon. Nevertheless, this increased accuracy comes at the price of increased mesh size, as the particle internal geometry has to be meshed, and increased CPU cost, as the two regions are solved in a segregated-coupled manner. Still, this additional complexity allows to tackle problems featuring internal resistance to heat transfer, i.e. particle with a Biot number higher than 0.1. In order to assess the possibility of neglecting internal heat transfer, three different setups were examined for a Reynolds number of 10. The first one features a Biot number far below 0.1, with both solid and fluid regions meshed. The second has a Biot number far below 0.1, with only the fluid region meshed. A constant particle temperature over the bed is assumed. Its purpose is to show that, indeed, for very low Biot number internal, heat transfer can be neglected. The third one has a Biot number of 0.6, and the actual thermal conductivity of wood is used: 0.1 W/m/K (51), with both solid and fluid regions meshed. This last setup illustrates the importance of internal heat resistance, especially in the case of biomass thermochemical conversion. A discussion on Biot number relevance in the case of a particle having a volumetric heat release is available in the appendix.

Figure 7 presents the fluid temperature averaged over a cross section over the bed height for the three setups. As one can see, in the case of a very low Biot number, both setups predict exactly the same values for the convective heat transfer coefficient. It is not surprising, as in these cases, the transfer resistance is located in the fluid and both solvers account for the fluid motion in the same way. Furthermore, the observed curves are close to the solution that could be derived analytically, i.e. first order increasing exponential trend reaching a plateau as conduction may play a significant role. The discrepancies arise when comparing those results to those obtained for a Biot number of 0.6. The fluid temperature increases steadily over the bed height until it reaches the same final value as in the low Biot number case. The fact that the final temperature values are the same in any configuration

$$\omega_p = 14.062 \, 10^6 \times 2.50 \, 10^9 \exp(-\frac{99800}{RT_p})(0.21 \times \rho_f)^{0.734}$$
$$\text{in W/m}^3 \quad \textbf{(11)}$$

In addition to being of practical relevance, the case of torrefied wood, self-heating 150 °C has two other desirable features. First, because of wood chips intermediate Biot number, chemical reaction and heat transfer cannot be decoupled. Furthermore, the chemistry involved is quite simple. Indeed, the diffusion of oxygen into 3 mm wood chips takes less than 1 second. The torrefaction phenomenon has a characteristic time of tens of minutes. Thus, oxygen concentration can be assumed uniform throughout the wood chip. In addition, in the case of the experiments we are comparing to, oxygen depletion across the bed was less than 1 % absolute. Thus, assuming constant oxygen density field seems is reasonable. More complex chemical reactions, such as multistep kinetics, could be added in the same way.
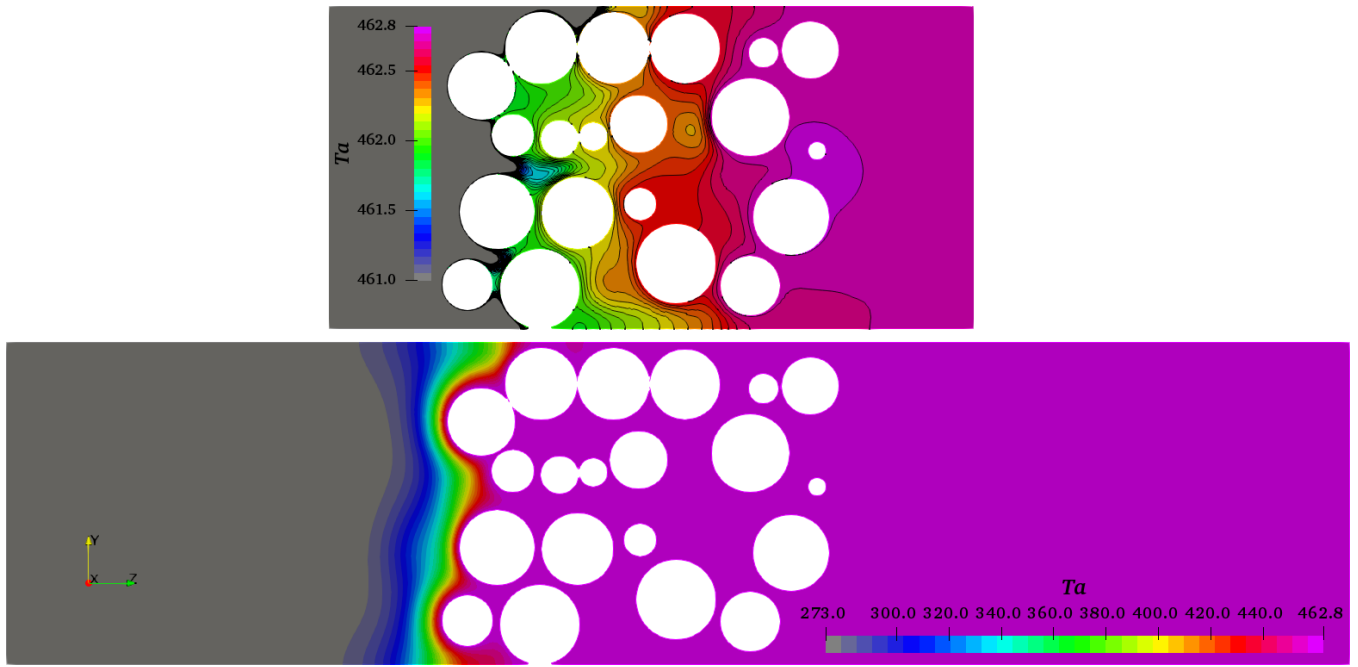
Fig. 5. Heat map in the fluid region. Case setup: 61 spheres of 3 mm diameter enclosed in a cylinder, Re = 10, $\omega = 10^6$ W/m^3, k_p = 100 W/m/K, fluid inlet temperature: air at 273 K, flow from left to right. Slice view along the streamwise axis. Upper part: detailed view of the bed
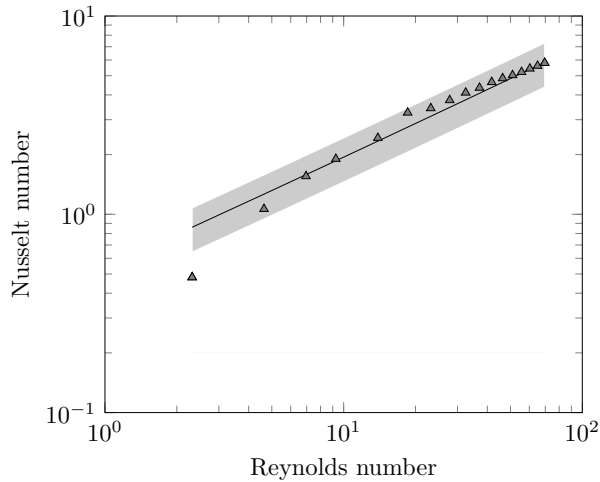

Fig. 6. Nusselt number computed versus Reynolds number for the case of a fixed bed with multiple spheres. Markers: presented solver. Continuous line: Whitaker's correlation. Shaded area: ± 25 % deviation over Whitaker's correlation
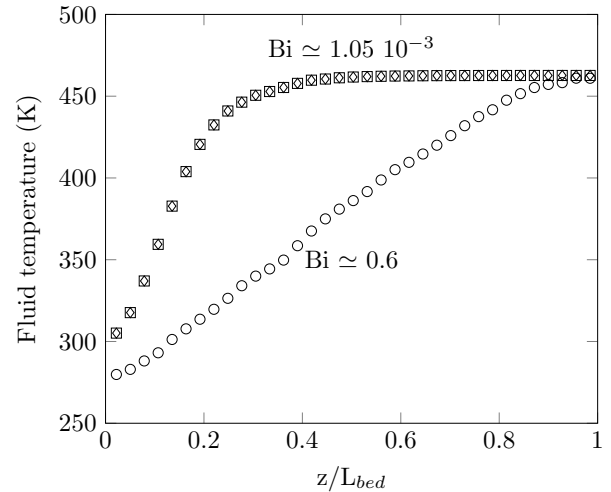

Fig. 7. Fluid temperature averaged over a cross section versus bed height. Diamonds: first setup (Biot far below 0.1, fluid and solid), squares: second setup (Biot far below 0.1, fluid only), circles: third setup (Biot above 0.1, fluid and solid)

5 1. Convective heat transfer coefficient

The first problem the proposed workflow can solve is to compute the effective heat transfer coefficient of the bed for different Reynolds number values. This parameter can be crucial for the industrial design of a bed, while it seems almost impossible to acquire experimentally for non-heat-conducive materials such as wood. Calculations were conducted with a constant heat source inside the chips corresponding to the magnitude reported by Bouzarour et al. (ω_p = 5.32 kW/m^3 at 150 °C). The computational domain is a volume sample of the numerically-generated packed bed of wood chips. The volume sample is a cube. Each edge is equal to 10 equivalent diameters (3x3x3 cm^3). It was taken more than 20 equivalent diameters away from the inlet to avoid packing alter-

ation (21 d_p < z < 31 d_p).This sampling geometry, which was chosen in previous work on fluid flow, showed that 8 equivalent diameters were enough to ensure convergence on the same topology (42). Furthermore, domain size is a quite stringent criterion, even in the case of fluid flow only, as improper evaluation of channeling would lead to dramatic loss of momentum. Adding heat transfer in the fluid domain does not change this statement. Indeed, as Peclet number is large in our case, convection evaluation is key, while conduction plays a minor role in this region. The four sides of the computational domain were specified as symmetry planes (slip condition for velocity and zero-gradient for pressure and temperatures). This procedure yielded a bed with a porosity of 0.47 and a specific surface area of 1276 m^2/m^3, two required

properties to compute the heat transfer coefficient using Eq. 10.

Four cases, with Reynolds numbers ranging from 1 to 10, were investigated. A point of note is that wood is an anisotropic material with a thermal conductivity ratio of about 2 between its longitudinal and tangential/azimuthal directions (54). For the sake of simplicity, and because chips orientation in the bed is random, wood thermal conductivity tensor was simplified into a simple scalar value of 0.1 W/m/K (51).

Figure 8 presents velocity and temperature variation $(T_p(z) - min(T_p(z)))$ at z = 27 d_p, Re = 10, across a bed of wood chips. Qualitatively, the velocity field exhibits channeling, not necessarily in the openness of the pores of this cut. This can be explained by the fact that channeling is the result of the geometry formerly encountered by the flow and the pressure drop ahead of it. Thus, it exhibits memory and forecast effects that cannot be accounted for in slice view. This observation agrees well with former investigations on the hydrodynamics of this type of packed bed (42). The chip temperature mapping reveals close interaction between the flow and heat transfer. Low velocity fluid zones are associated with higher chip temperature, namely hot spots. It can be concluded that the workflow computations are in agreement with intuitive expectations. More quantitatively, Table 4 reports the values of the heat transfer coefficient. They were obtained by fitting temperature profiles with a 1D bed described with equivalent physical properties as advised by Wakao (48). In terms of general trend, the workflow reports an increase of the heat transfer coefficient with Reynolds. Still, values are constant for low Reynolds numbers (1 and 2) and only moderately increase afterwards. This observation is counter-intuitive and calls for an explanation. Section 4 showed that both solid and fluid thermal resistances were considered in this problem. While the solid resistance is constant, the fluid one is depending on velocity and should decrease as velocity increases. Still as shown here and in (42, 55), this type of packed bed is very prone to channeling. Below a particle Reynolds number value of 5, the flow is in Darcy's regime. This has two consequences: 1. the flow patterns are identical and velocity scales with the flow rate; 2. in terms of heat transfer, in the flow channels the local fluid heat transfer resistance is low and any increase in the flow velocity decreases it even further. Still, in these zones, the resistance limiting heat transfer is the solid one. Thus, no improvement of overall heat transfer performance is observed as only the fluid resistance decreases. This explains the trend observed at low Reynolds values. Going to higher Reynolds numbers modifies the flow structures. This was explored by comparing normalized velocity distributions $\|u(z)\|/\|u_{in}\|$ - (Fig. 9). As one can see, by increasing the Reynolds number from 5 to 10, the flow pattern is enhanced around the particle walls everywhere in the bed. This promotes heat transfer in zones where the limiting resistance is the fluid one and explain the reported increased heat transfer coefficient.
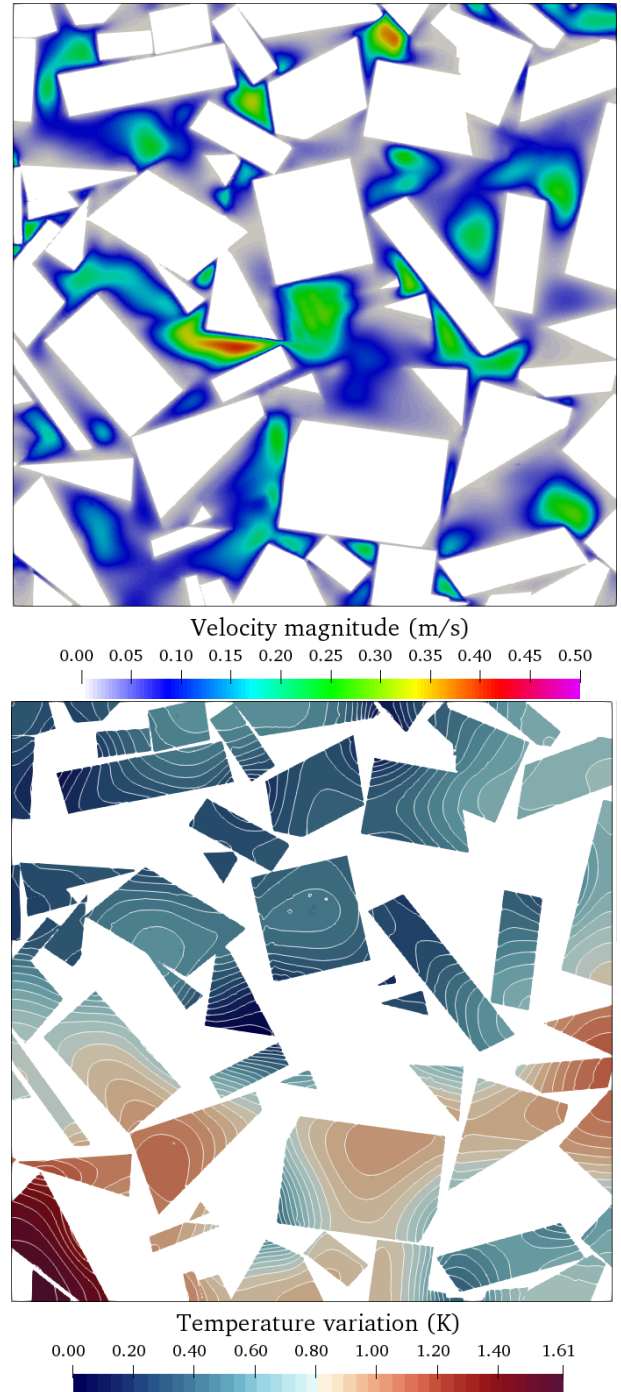

Fig. 8. Velocity (top) and temperature variation (bottom, T(z) - min(T(z)) at z = 27 d_p, Re = 10 across a wood chip bed under constant heat source of 5.32 kW/m^3

5 2. Hot spots and thermal runaway

The proposed workflow is not limited to convective heat transfer coefficient determination. As a next step to this work, the heat map heterogeneity across the bed is examined. Figure 8 presents a slice view of the wood chips temperature field (z = 27 d_p and Re = 10). The chips temperature is distributed. Industrially, temperature distribution can lead to differences in substrate thermal treatment and consequently to the end product. As it has been shown, altering velocity influences not only flow patterns but also thermal behavior. It is

Fluid velocity at 150 °C (mm/s)	Particle Reynolds	Bed Reynolds	h (W/m²/K)	Nusselt
2.5	1	2.27	4.88	0.87
5.0	2	4.55	4.72	0.85
12.5	5	11.36	5.78	1.04
25.0	10	22.73	7.65	1.37

Table 4. Heat transfer coefficient as a function of Reynolds number in the wood chip packed bed
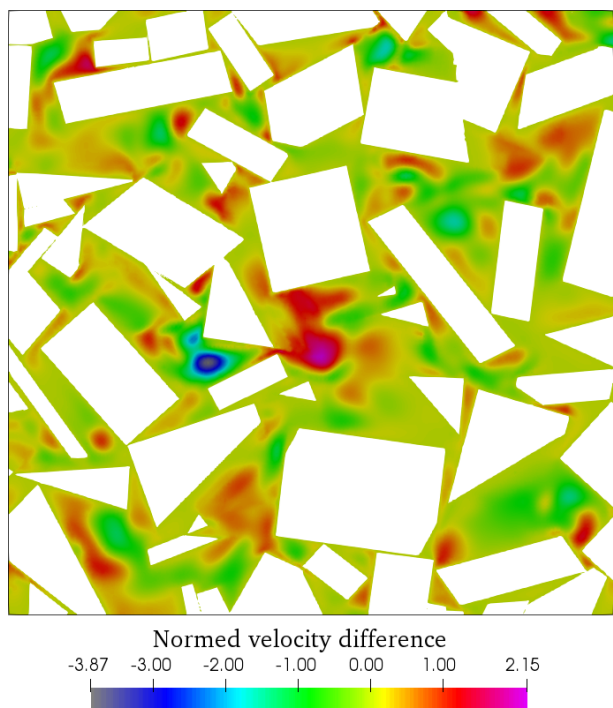

Fig. 9. Normed velocity ($\|\boldsymbol{u}(\boldsymbol{z})\|/\|\boldsymbol{u}_{in}\|$) difference between flows at Reynolds 10 and 5, at z = 27 d_p

Fig. 10. Chips temperature distribution around the averaged value at z = 27 d_p. Black line: Reynolds number value of 5, gray line: Reynolds number value of 10

also possible to plot temperature distribution across the chips. Figure 10 reports the temperature distribution around its averaged value for two cases: Reynolds number of 5 and 10, at 27 d_p from the inlet. From this graph, it can be concluded that increasing the Reynolds number from 5 to 10, decreased the spread of the temperature field and suppressed high intensity outliers (+1 and -1 K for the case of Reynolds number equal to 5). From a more general perspective, the workflow allows to extract both global and local observations for both fluid and solid phases.

As mentioned earlier, during their cooldown, torrefied wood chips can be subject to self-heating, and, in the most extreme cases, thermal runaway. In order to account for it, the heat source term inside the particles was treated as temperature-dependent (Eq. 11). Once implemented, the upgraded code predictions were examined with respect to experimental observations. Table 5 summarizes those findings. The code does not predict a thermal runaway per se, which would have led to numerical divergence. Such divergence was also experienced by starting the simulation at a higher temperature. Still, the code predicts temperature rise over the 10 d_p height of the bed. As one can see, the predicted trend is non-linear as a multiple of 3 of the flow rate (from 10 to 30
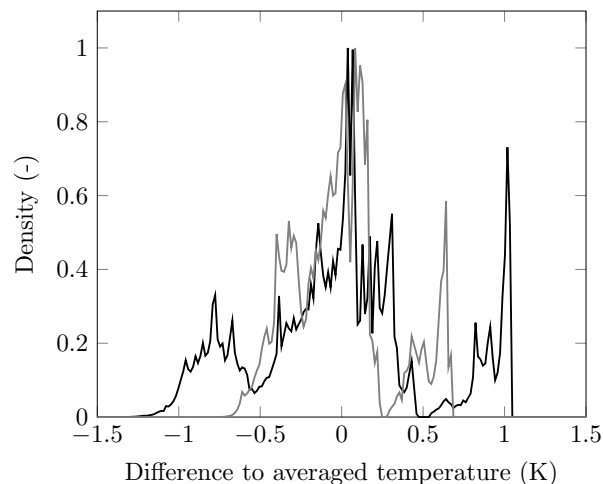
Nl/min) divided by the temperature increase by 4.6. Furthermore, extrapolating those local results obtained on 10 d_p to a 100 d_p bed is not easy. Yet, linear scaling may yield simplistic estimations. The lowest flow rate (10 Nl/min) would yield a 360 K temperature rise which could be considered as thermal runaway. The intermediate flow rate (20 Nl/min) would yield 128 K increase, which can also be considered as thermal runaway. Finally, the highest flow rate (30 Nl/min) would induce a 78 K rise, which can be seen as strong self-heating and surely as thermal runaway. This highlights one of the limitations of the proposed workflow. As it relies on a local approach, it can yield many interesting observations but requires an upscaling procedure to predict the behavior of larger beds. In addition, being operated in steady-state, it cannot account for substrate deactivation over time. These two developments could be accomplished by using a simple 1D code powered by the local heat transfer coefficients (Table. 4).

6. Conclusion and perspectives

This article presents a numerical workflow capable of characterising heat transfer inside a packed bed. First, the bed is generated numerically using a DEM code. Then, a classical computational fluid dynamic approach is used to acquire flow patterns inside the pores of the bed. Finally, heat conservation equation is solved in both fluid and solid regions in a coupled manner. Thorough validation was conducted against well-established experimental results. Next, the possibility to neglect solid phase resistance in low Biot number configurations was demonstrated. Finally, the workflow was used

Experimental flow rate (NL/min)	Velocity (mm/s – at 150 °C)	Experimental observations	Numerical temperature rise over $10\,d_p$
10	8.10	Thermal runaway	12.0 K
20	16.3	Thermal runaway (near z = 30 cm)	4.28 K
30	25.0	Stable condition	2.61 K

Table 5. Experimental and numerical observations (equivalent values, not computed).

to gain insight on heat transfer inside a torrefied wood chips packed bed. First, from a practical perspective, values of heat transfer coefficient have been obtained for such complex geometries. This investigation was carried out for an intermediate Biot number of 0.6, where a classical approach based on decoupling between phenomena cannot be used. It revealed that channeling is key in understanding heat transfers in this type of beds and allowed to quantify the magnitude of its effects on the temperature field of the chips.

From a wider perceptive, the proposed workflow paves the way to a new research horizon. Indeed, the CFD solution gives insight to local information. For example, preliminary results indicate that the coefficient increases linearly through the first layer of particles and later presents large variations depending on the local channeling effects. By implementing wood anisotropy at the chip level, it would be possible to assess the validity of assuming macroscopic isotropy of the bed, owing respect to their random packing. Another perspective is to use these tools to pack several times the chip beds and assess the heat transfer coefficient in each case. Hence, its variability could be assessed, giving a constraint on the maximal accuracy to expect from correlations and single experiment results. This will eventually give guidelines on the particle size distribution that reduces risks of runaway at the lowest wood grinding cost.

The interested reader can download the solver and test case from our git repository. Furthermore, as the geometry is imported via stl file, the reader could use its own, no matter how complex.

Acknowledgement

Latin symbols

a	specific surface area	m^2/m^3
c_p	specific heat	J/kg/K
d	diameter	m
g	gravity acceleration	m/s^2
h	convective heat transfer coefficient	$W/m^2/K$
k	heat conductivity	W/m/K
L	length	m
$\boldsymbol{n}$	surface normal vector	-
P	pressure	Pa
Pr	Prandtl number	-
Q	volumetric flow rate	m^3/s
$Re = \frac{d_p\|\boldsymbol{u}\|}{\nu}$	sphere Reynolds number	-
$Re = \frac{d_p\|\boldsymbol{u}\|}{\nu(1-\epsilon)}$	bed or Whitaker Reynolds number	-
S	surface	m^2
$\boldsymbol{u}$	superficial velocity	m/s
T	temperature	K
V	volume	m^3
x	abscissa	m

Greek symbols

ϵ	porosity	-
ρ	density	kg/m^3
ω	heat release	W/m^3
ν	kinematic viscosity	m^2/s

Subscripts

bed	bed
f	fluid
in	inlet
out	outlet
p	particle

Other symbols

∇	nabla operator
Δ	difference operator
Δ^*	log mean difference operator
$\|\boldsymbol{a}\|$	norm of $\boldsymbol{a}$
$\bar{a}$	arithmetic average

Table 6. Nomenclature

References

1. A. V Bridgwater. Renewable fuels and chemicals by thermal processing of biomass. *Chemical Engineering Journal*, 91(2):87–102, March 2003. ISSN 1385-8947. .

2. T. Damartzis and A. Zabaniotou. Thermochemical conversion of biomass to second generation biofuels through integrated process design—A review. *Renewable and Sustainable Energy Reviews*, 15(1):366–378, January 2011. ISSN 1364-0321. .

3. Berta Matas Güell, Judit Sandquist, and Lars Sørum. Gasification of Biomass to Second Generation Biofuels: A Review. *Journal of Energy Resources Technology*, 135(1), March 2013. ISSN 0195-0738. .

4. Tao Kan, Vladimir Strezov, and Tim J. Evans. Lignocellulosic biomass pyrolysis: A review of product properties and effects of pyrolysis parameters. *Renewable and Sustainable Energy Reviews*, 57:1126–1140, May 2016. ISSN 1364-0321. .

5. Bimal Acharya, Animesh Dutta, and Jamie Minaret. Review on comparative study of dry and wet torrefaction. *Sustainable Energy Technologies and Assessments*, 12:26–37, December 2015. ISSN 2213-1388. .

6. A. Sarvaramini, Gnouyaro P. Assima, and F. Larachi. Dry torrefaction of biomass – Torrefied products and torrefaction kinetics using the distributed activation energy model. *Chemical Engineering Journal*, 229:498–507, August 2013. ISSN 1385-8947. .

7. Anjireddy Bhavanam and RC Sastry. Biomass gasification processes in downd raft fixed bed reactors: a review. *International Journal of Chemical Engineering and Applications*, 2 (6):425, 2011. ISSN 2010-0221.

8. S. Chopra and A. Jain. A review of Fixed Bed Gasification Systems for Biomass. April 2007. ISSN 1682-1130.

9. Siyi Luo, Yangmin Zhou, and Chuijie Yi. Syngas production by catalytic steam gasification of municipal solid waste in fixed-bed reactor. *Energy*, 44(1):391–395, August 2012. ISSN 0360-5442. .

10. Chong Chen, Yu-Qi Jin, Jian-Hua Yan, and Yong Chi. Simulation of municipal solid waste gasification in two different types of fixed bed reactors. *Fuel*, 103:58–63, January 2013. ISSN 0016-2361. .

11. Yann Le Brech, Liangyuan Jia, Sadio Cissé, Guillain Mauviel, Nicolas Brosse, and Anthony Dufour. Mechanisms of biomass pyrolysis studied by combining a fixed bed reactor with advanced gas analysis. *Journal of Analytical and Applied Pyrolysis*, 117:334–346, January 2016. ISSN 0165-2370. .

12. A. M. Mastral, R. Murillo, M. S. Callén, T. García, and C. E. Snape. Influence of Process Variables on Oils from Tire Pyrolysis and Hydropyrolysis in a Swept Fixed Bed Reactor.

Energy & Fuels, 14(4):739–744, July 2000. ISSN 0887-0624. .

13. S. Monteiro Nunes, N. Paterson, A. A. Herod, D. R. Dugwell, and R. Kandiyoti. Tar Formation and Destruction in a Fixed Bed Reactor Simulating Downdraft Gasification: Optimization of Conditions. *Energy & Fuels*, 22(3):1955–1964, May 2008. ISSN 0887-0624. .

14. Vimal R. Patel, Darshit S. Upadhyay, and Rajesh N. Patel. Gasification of lignite in a fixed bed reactor: Influence of particle size on performance of downdraft gasifier. *Energy*, 78: 323–332, December 2014. ISSN 0360-5442. .

15. Élizabeth Trudel, William L. H. Hallett, Evan Wiens, Jeremiah D. O'Neil, Marina K. Busigin, and Dana Berdusco. Fuel particle shape effects in the packed bed combustion of wood. *Combustion and Flame*, 198:100–111, December 2018. ISSN 0010-2180. .

16. Brieuc Evangelista, Patricia Arlabosse, Alexandre Govin, Sylvain Salvador, Olivier Bonnefoy, and Jean-Louis Dirion. Reactor scale study of self-heating and self-ignition of torrefied wood in contact with oxygen. *Fuel*, 214:590–596, February 2018. ISSN 0016-2361. .

17. Nicolas Piatkowski and Aldo Steinfeld. Solar-driven coal gasification in a thermally irradiated packed-bed reactor. *Energy & Fuels*, 22(3):2043–2052, June 2008. ISSN 0887-0624. . WOS:000256057600086.

18. Zhiyi Yao, Xin He, Qiang Hu, Wei Cheng, Haiping Yang, and Chi-Hwa Wang. A hybrid peripheral fragmentation and shrinking-core model for fixed-bed biomass gasification. *Chemical Engineering Journal*, 400:124940, November 2020. ISSN 1385-8947. .

19. Chekib Ghabi, Hmaied Benticha, and Mohamed Sassi. Two-Dimensional Computational Modeling and Simulation of Wood Particles Pyrolysis in a Fixed Bed Reactor. *Combustion Science and Technology*, 180(5):833–853, April 2008. ISSN 0010-2202. .

20. Colomba Di Blasi. Modeling wood gasification in a countercurrent fixed-bed reactor. *AIChE Journal*, 50(9):2306–2319, 2004. ISSN 1547-5905. .

21. Souad Messai, Mohamed El Ganaoui, Jalila Sghaier, Laurent Chrusciel, and Gabsi Slimane. Comparison of 1D and 2D models predicting a packed bed drying. *International Journal for Simulation and Multidisciplinary Design Optimization*, 5:A14, 2014. ISSN 1779-627X, 1779-6288. .

22. Stephen Whitaker. Forced convection heat transfer correlations for flow in pipes, past flat plates, single cylinders, single spheres, and for flow in packed beds and tube bundles. *AIChE Journal*, 18(2):361–371, March 1972. ISSN 0001-1541. .

23. Paola Ranut, Enrico Nobile, and Lucia Mancini. High resolution X-ray microtomography-based CFD simulation for the characterization of flow permeability and effective thermal conductivity of aluminum metal foams. *Experimental Thermal and Fluid Science*, 67:30–36, October 2015. ISSN 0894-1777. .

24. S. Jaganathan, H. Vahedi Tafreshi, and B. Pourdeyhimi. A realistic approach for modeling permeability of fibrous media: 3-D imaging coupled with CFD simulation. *Chemical Engineering Science*, 63(1):244–252, January 2008. ISSN 0009-2509. .

25. Romain Guibert, Pierre Horgue, Gérald Debenest, and Michel Quintard. A Comparison of Various Methods for the Numerical Evaluation of Porous Media Permeability Tensors from Pore-Scale Geometry. *Mathematical Geosciences*, 48(3):329–347, April 2016. ISSN 1874-8961, 1874-8953. .

26. Sumit Kumar Singh, Manoj Kumar, Alok Kumar, Abhishek Gautam, and Sunil Chamoli. Thermal and friction characteristics of a circular tube fitted with perforated hollow circular cylinder inserts. *Applied Thermal Engineering*, 130:230–241, February 2018. ISSN 1359-4311. .

27. Sunil Chamoli, Ruixin Lu, Jin Xie, and Peng Yu. Numerical study on flow structure and heat transfer in a circular tube integrated with novel anchor shaped inserts. *Applied Thermal Engineering*, 135:304–324, May 2018. ISSN 1359-4311. .

28. Sinthuran Jegatheeswaran, Farhad Ein-Mozaffari, and Jiangning Wu. Process intensification in a chaotic SMX static mixer to achieve an energy-efficient mixing operation of non-newtonian fluids. *Chemical Engineering and Processing - Process Intensification*, 124:1–10, February 2018. ISSN 0255-2701. .

29. Nico Jurtz, Matthias Kraume, and Gregor D. Wehinger. Advances in fixed-bed reactor modeling using particle-resolved computational fluid dynamics (CFD). *Reviews in Chemical Engineering*, 35(2):139–190, 2019. ISSN 2191-0235. .

30. Chengzhi Hu, Mingrui Sun, Zhiyong Xie, Lei Yang, Yongchen Song, Dawei Tang, and Jiafei Zhao. Numerical simulation on the forced convection heat transfer of porous medium for turbine engine heat exchanger applications. *Applied Thermal Engineering*, 180:115845, November 2020. ISSN 1359-4311. .

31. Sebastian Meinicke, Konrad Dubil, Thomas Wetzel, and Benjamin Dietrich. Characterization of heat transfer in consolidated, highly porous media using a hybrid-scale CFD approach. *International Journal of Heat and Mass Transfer*, 149:119201, March 2020. ISSN 0017-9310. .

32. Gianluca Boccardo, Frédéric Augier, Yacine Haroun, Daniel Ferré, and Daniele L. Marchisio. Validation of a novel open-source work-flow for the simulation of packed-bed reactors. *Chemical Engineering Journal*, 279:809–820, November 2015. ISSN 1385-8947. .

33. Behnam Partopour and Anthony G. Dixon. An integrated workflow for resolved-particle packed bed models with complex particle shapes. *Powder Technology*, 322:258–272, December 2017. ISSN 0032-5910. .

34. Stepan A. Mikhailenko and Mikhail A. Sheremet. Impacts of rotation and local element of variable heat generation on convective heat transfer in a partially porous cavity using local thermal non-equilibrium model. *International Journal of Thermal Sciences*, 155:106427, September 2020. ISSN 1290-0729. .

35. U. S. Mahabaleshwar, K. R. Nagaraju, P. N. Vinay Kumar, M. N. Nadagouda, R. Bennacer, and M. A. Sheremet. Effects of Dufour and Soret mechanisms on MHD mixed convective-radiative non-Newtonian liquid flow and heat transfer over a porous sheet. *Thermal Science and Engineering Progress*, 16:100459, May 2020. ISSN 2451-9049. .

36. Pierre-Lou Billerot, Louis Dufresne, Romain Lemaire, and Patrice Seers. 3D CFD analysis of a diamond lattice-based porous burner. *Energy*, 207:118160, September 2020. ISSN 0360-5442. .

37. G. M. Karthik and Vivek V. Buwa. Effect of particle shape on catalyst deactivation using particle-resolved CFD simulations. *Chemical Engineering Journal*, 377:120164, December 2019. ISSN 1385-8947. .

38. Peter A Cundall and Otto DL Strack. A discrete numerical model for granular assemblies. *Geotechnique*, 29(1):47–65, 1979. ISSN 0016-8505.

39. E.G. Gilbert, D.W. Johnson, and S.S. Keerthi. A fast procedure for computing the distance between complex objects in three-dimensional space. *IEEE Journal on Robotics and Automation*, 4(2):193–203, April 1988. ISSN 0882-4967, 2374-8710. .

40. Anthony Wachs, Laurence Girolami, Guillaume Vinay, and Gilles Ferrer. Grains3D, a flexible DEM approach for particles of arbitrary convex shape — Part I: Numerical model and validations. *Powder Technology*, 224:374–389, July 2012. ISSN 0032-5910. .

41. Matthieu Rolland, Andriarimina Daniel Rakotonirina, Anaïs Devouassoux, José Luis Barrios Goicetty, Jean-Yves Delenne, and Anthony Wachs. Predicting Average Void Fraction and Void Fraction Uncertainty in Fixed Beds of Poly Lobed Particles. *Industrial & Engineering Chemistry Research*, 58(9):3902–3911, March 2019. ISSN 0888-5885. .

42. V. Pozzobon, J. Colin, and P. Perré. Hydrodynamics of a packed bed of non-spherical polydisperse particles: A fully virtual approach validated by experiments. *Chemical Engineering Journal*, 354:126–136, 2018.

43. Frédéric Dubois, Michel Jean, Mathieu Renouf, Rémy Mozul, Alexandre Martin, and Marine Bagneris. Lmgc90. In *10e colloque national en calcul des structures*, page Clé USB, 2011.

44. T. J. Donohue and C. M. Wensrich. A numerical investigation of the void structure of fibrous materials. *Powder Technology*, 186(1):72–79, August 2008. ISSN 0032-5910. .

45. Hrvoje Jasak, Aleksandar Jemcov, and Zeljko Tukovic. OpenFOAM: A C++ library for complex physics simulations. In *International workshop on coupled methods in numerical dynamics*, volume 1000, pages 1–20. IUC Dubrovnik, Croatia, 2007.

46. D. S. Jang, R. Jetli, and S. Acharya. Comparison of the Piso, Simpler, and Simplec Algorithms for the Treatment of the Pressure-Velocity Coupling in Steady Flow Problems. *Numerical Heat Transfer*, 10(3):209–228, September 1986. ISSN 0149-5720. . Publisher: Taylor & Francis _eprint: https://doi.org/10.1080/10407788608913517.

47. Roland Clift, John R Grace, and Martin E Weber. *Bubbles, drops, and particles*. Courier Corporation, 2005. ISBN 0-486-44580-1.

48. N. Wakao, S. Kaguei, and T. Funazkri. Effect of fluid dispersion coefficients on particle-to-fluid heat transfer coefficients in packed beds: Correlation of nusselt numbers. *Chemical Engineering Science*, 34(3):325–336, January 1979. ISSN 0009-2509. .

49. Zhi-Gang Feng and Efstathios E. Michaelides. A numerical study on the transient heat transfer from a sphere at high Reynolds and Peclet numbers. *International Journal of Heat and Mass Transfer*, 43(2):219–229, January 2000. ISSN 0017-9310. .

50. WE Ranz and W R_ Marshall. Evaporation from drops. *Chem. eng. prog*, 48(3):141–146, 1952.

51. R. S. Miller and J. Bellan. Analysis of reaction products and conversion time in the pyrolysis of cellulose and wood particles. *Combustion Science and Technology*, 119(1-6):331–373, 1996. ISSN 0010-2202. . A1996WP80000015.

52. A. Bouzarour, V. Pozzobon, P. Perré, and S. Salvador. Experimental study of torrefied wood fixed bed: Thermal analysis and source term identification. *Fuel*, 234:247–255, 2018.

53. Nicolas St-Pierre, Annie Brégard, and Valérie Bélanger. *Ventilation et conservation des grains à la ferme*. Réseau Innovagrains, 2014. ISBN 2-7649-0486-X.

54. G. Leon, J. Cruz-de Leon, and L. Villasenor. Thermal characterization of pine wood by photoacoustic and photothermal techniques. *Holz als Roh- und Werkstoff*, 58(4):241–246, November 2000. ISSN 1436-736X. .

55. Neil T. M. Duffy and John A. Eaton. Investigation of factors affecting channelling in fixed-bed solid fuel combustion using CFD. *Combustion and Flame*, 160(10):2204–2220, October 2013. ISSN 0010-2180. .